This article was downloaded by: [University of California, San Diego]
On: 17 November 2014, At: 17:42
Publisher: Taylor & Francis
Informa Ltd Registered in England and Wales Registered Number: 1072954 Registered office: Mortimer House, 37-41 Mortimer Street, London W1T 3JH, UK

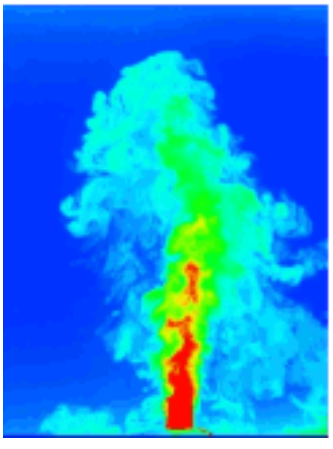

Journal of Turbulence
Publication details, including instructions for authors and subscription information:
http://www.tandfonline.com/loi/tjot20

Transport and mixing of density in a continuously stratified shear layer

Hieu T. Pham [a] & Sutanu Sarkar [a]
[a] Department of Mechanical and Aerospace Engineering , University of California, San Diego , La Jolla, CA, USA
Published online: 29 Jun 2010.

To cite this article: Hieu T. Pham & Sutanu Sarkar (2010) Transport and mixing of density in a continuously stratified shear layer, Journal of Turbulence, 11, N24, DOI: 10.1080/14685248.2010.493560

To link to this article: http://dx.doi.org/10.1080/14685248.2010.493560

PLEASE SCROLL DOWN FOR ARTICLE

Taylor & Francis makes every effort to ensure the accuracy of all the information (the "Content") contained in the publications on our platform. However, Taylor & Francis, our agents, and our licensors make no representations or warranties whatsoever as to the accuracy, completeness, or suitability for any purpose of the Content. Any opinions and views expressed in this publication are the opinions and views of the authors, and are not the views of or endorsed by Taylor & Francis. The accuracy of the Content should not be relied upon and should be independently verified with primary sources of information. Taylor and Francis shall not be liable for any losses, actions, claims, proceedings, demands, costs, expenses, damages, and other liabilities whatsoever or howsoever caused arising directly or indirectly in connection with, in relation to or arising out of the use of the Content.

This article may be used for research, teaching, and private study purposes. Any substantial or systematic reproduction, redistribution, reselling, loan, sub-licensing, systematic supply, or distribution in any form to anyone is expressly forbidden. Terms & Conditions of access and use can be found at http://www.tandfonline.com/page/terms-and-conditions

Journal of Turbulence
Vol. 11, No. 24, 2010, 1–23

Taylor & Francis
Taylor & Francis Group

Transport and mixing of density in a continuously stratified shear layer

Hieu T. Pham and Sutanu Sarkar*

Department of Mechanical and Aerospace Engineering, University of California, San Diego, La Jolla, CA, USA

(*Received 3 January 2010; final version received 30 April 2010*)

Scalar transport and mixing by active turbulence in a high Reynolds number inhomogeneous stratified shear layer are investigated using three-dimensional Direct Numerical Simulation. Two density profiles are considered: (i) two layers of homogenous fluid with different density, namely the two-layer case, and (ii) a continuously stratified background ambient, namely the J_d case. The evolution of the mixing layer includes shear instability, formation of Kelvin–Helmholtz rollers, transition to turbulence, fully developed active turbulence, and, finally, decay toward a laminar state. In the J_d case, internal gravity waves carrying momentum and energy are observed to propagate away from the shear layer. Although different during the initial evolution, the eddy diffusivity and mixing efficiency when plotted as a function of buoyancy, Reynolds number takes similar values between the two cases later in time during the stage when turbulence decays. During this stage, the mixing efficiency computed based on the buoyancy flux is approximately 0.35, while the mixing efficiency estimated from the scalar dissipation is approximately 0.4. Parameterization of the eddy diffusivity in terms of Reynolds numbers and gradient Richardson number is also discussed.

Keywords: stratified shear layer; turbulence; internal waves

Downloaded by [University of California, San Diego] at 17:42 17 November 2014

1. Introduction

In the past decades, turbulent mixing in a stratified fluid driven by a background shear has been one of the focal research topics in terms of understanding the mechanism of mixing as well as its parameterization in models of large-scale environmental flows. Although there has been much progress [1–3], a number of unresolved questions remain, including the following: (i) the interaction of internal gravity waves that can transport significant amount of momentum and energy to the ambient, with local mixing, and (ii) the influence of Reynolds number (Re). These issues are addressed by the current study that utilizes three-dimensional (3D) Direct Numerical Simulation (DNS) to investigate turbulent mixing in a high Re shear layer in a continuously stratified ambient where internal waves are supported.

Turbulent mixing in homogenous flows has been thoroughly investigated including parameterization schemes for mixing. Jacobitz et al. [4] use 3D-DNS to study turbulence mixing in a periodic box with constant vertical shear S in a linearly stratified ambient where stratification is measured by squared buoyancy frequency $N^2 = (-g/\rho_0)d\langle\rho\rangle/dz$. The turbulence evolution is found to strongly depend on the gradient Richardson number $Ri_g = N^2/S^2$, the Reynolds numbers defined using the Taylor microscale, and the shear

*Corresponding author. Email: sarkar@ucsd.edu

ISSN: 1468-5248 online only
© 2010 Taylor & Francis
DOI: 10.1080/14685248.2010.493560
http://www.informaworld.com

number SK/ε, where K is the Turbulent Kinetic Energy (TKE) and ε is the dissipation rate. Riley and deBruynKops [5] investigate the properties of turbulent mixing driven by Taylor–Green vortices. The mixing efficiency is large initially and settles down to the value of approximately 0.4 during the turbulence decay period. Shih et al. [6] investigate the parameterization of eddy viscosity and eddy diffusivity using simulations of homogenous shear flow with stratification. The evolution of the eddy diffusivity is found to consist of three regimes: energetic, intermediate, and diffusive mixing. There is a strong dependence of eddy diffusivity on the turbulence activity $\varepsilon/(\nu N^2)$, also known as buoyancy Reynolds number Re_b. Other parameterizations using the parameters $ReFr_k^2$ and Re/Ri_g are also shown to describe the evolution of eddy diffusivity. Here $Re = q\Lambda/\nu$, where $q = \sqrt{(2K)}$, Λ is the integral lengthscale, and $Fr_k = \varepsilon/(NK)$ is the local Froude number.

Turbulent mixing, in a two-layer shear flow with hyperbolic tangent density and velocity profiles has received significant attention. Caulfield and Peltier [7] use stability analysis and 3D-DNS to identify, in addition to the primary Kelvin–Helmhotlz (K–H) shear instability, a secondary instability wherein streamwise vortices are formed at the braids, interact with each other, and thus drive the mixing. The secondary instability is also observed in the 3D-DNS of Werne et al. [8]. Staquet [9] from 3D-DNS studies describes three stages of mixing: the first stage of primarily 2D K–H instability with high mixing efficiency, the second stage of small-scale 3D instability as in the work of Caulfield and Peltier [7], and the final stage of turbulence generation and decay in which the flux Richarson number approaches the value of approximately 0.25. In the final stage, the eddy diffusivity exhibits an inverse dependence on the gradient Richardson number Ri_g, which is defined using the sorted background density profile as introduced by Winters et al. [10]. Smyth et al. [11–13] investigate the effect of Re and Prandtl number Pr upon the evolution of the mixing event and further contrast their 3D-DNS results to the observed mixing data in the equatorial undercurrents. Upon comparison, they conclude that the DNS results agree well with the data from field observations. They further state that the age of a turbulent mixing event can be described by the ratio $R_{OT} = L_O/(L_E^{3/4}L_T^{1/4})$, where L_0, L_E, and L_T are the Ozmidov, Ellison, and Thorpe scales, respectively. The mixing efficiency is found to be in the range of 0.2–0.6.

Turbulent mixing with a background shear and a density profile different from the two-layer problem has been studied. Strang and Fernando [14] perform a laboratory experiment to investigate the turbulent entrainment at a sheared density interface. The background condition is a stratified shear layer situated between a well-mixed turbulent upper layer and a quiescent linearly stratified lower layer. The flow evolution includes K–H instability and a secondary *Hölmböe* wave instability whose interactions with each other can cause breaking and intense mixing. Internal waves are observed to propagate into the lower region. The proportion of the wave energy flux to the rate of change of potential energy due to mixed-layer deepening is approximately 48%. Tse et al. [15] uses 3D-DNS to study the evolution of stratified turbulence in a forced jet, a model for the atmospheric tropopause. The jet is maintained at quasi-equilibrium state with strong turbulence in the core, and patchy turbulence and nonlinear internal waves at the edges. It is found that spatial variation in turbulence activity across the jet can be characterized through length scales and budget equations for the velocity and density variances.

Internal waves excited by an unstable shear layer have been observed to carry significant momemtum flux. Sutherland and Linden [16] perform a laboratory experiment in which a thin vertical barrier is put inside a water channel and partially obstructs the incoming flow. The fluid is lightly stratified in the upper region while the lower region is strongly stratified. Vortices, shed in the wake of the barrier, excite internal waves. The waves propagating into

Downloaded by [University of California, San Diego] at 17:42 17 November 2014

the lower region are found to carry approximately 7% of the average momentum across the shear depth. Pham et al. [17] investigate the properties of the internal waves through 3D-DNS of a stratified shear layer at $Re = 1280$. The internal waves are excited by an unstable shear layer located between a weakly stratified region and a region with stronger stratification. The internal waves are found to carry up to 10% of the initial momentum in the shear layer. Integration of the TKE budget over the shear layer and time shows that the wave energy flux can be up to 17% of the turbulent production, 33% of the dissipation rate, and 75% of the buoyancy flux. The mixing efficiency is approximately 0.4.

Different from the work of Pham et al. [17], whose focus is on the properties of the large-scale internal waves radiated by the shear layer, the current investigation focuses on turbulent mixing inside the shear layer. The Reynolds number, $Re = 5000$ is nearly four times larger relative to [17]. Furthermore, in the current work, the largest turbulent activity $\varepsilon/(\nu N^2)$ is as large as 200 so that the turbulent mixing spans the entire three regimes according to Shih et al. [6]. Specifically, we aim to answer the following questions: (1) How does the presence of the external stratification and the excitation of internal gravity waves affect transport and mixing inside the shear layer? (2) How well can parameterization schemes in homogeneous stratified flows be applied toward parameterizing inhomogeneous stratified turbulence?

Downloaded by [University of California, San Diego] at 17:42 17 November 2014

2. Methods

3D-DNS are employed to describe the evolution of inhomogeneous stratified turbulence that originates from shear instability. The flow is a temporally evolving shear layer with the initial velocity having the following profile at $t = 0$:

$$\langle u^* \rangle(z, t = 0) = \frac{-\Delta U^*}{2} tanh\left(\frac{z^*}{0.5\delta^*_{\omega,0}}\right),$$

where ΔU^* is the velocity difference across the shear layer and $\delta^*_{\omega,0} = \Delta U^*/(d\langle u^* \rangle/dz^*)_{max}$ is the initial vorticity thickness. Subscript 0 indicates quantities at initial state, superscript $*$ denotes dimensional quantities, and the bracket $\langle \cdot \rangle$ indicates horizontal x–y average. Two types of initial density profiles are targeted. The first, namely the two-layer (2L) case, corresponds to the classical Thorpe experiments with the following profile at $t = 0$,

$$\langle \rho^* \rangle = \langle \rho^*_0 \rangle - \frac{\Delta \rho^*}{2} tanh\left(\frac{z^*}{0.5\delta^*_{\omega,0}}\right),$$

where $\Delta\rho^*$ is the density difference across twice the initial vorticity thickness $\delta^*_{\omega,0}$. The second, namely the J_d case, is continuously stratified with the following stratification profile at $t = 0$:

$$J(z) = \frac{J_s + J_d}{2} + \frac{J_s - J_d}{2} tanh\left(\frac{z^* + 2.5\delta^*_{\omega,0}}{\delta^*_{\omega,0}}\right).$$

Here, $J(z) = N(z)^{*2}\, \delta^{*2}_{\omega,0}/\Delta U^{*2}$ is the non-dimensional Richardson number with the buoyancy frequency $N^{*2} = -(g^*/\rho^*_0) d\langle \rho^* \rangle / dz^*$. J_s is chosen such that the density difference,

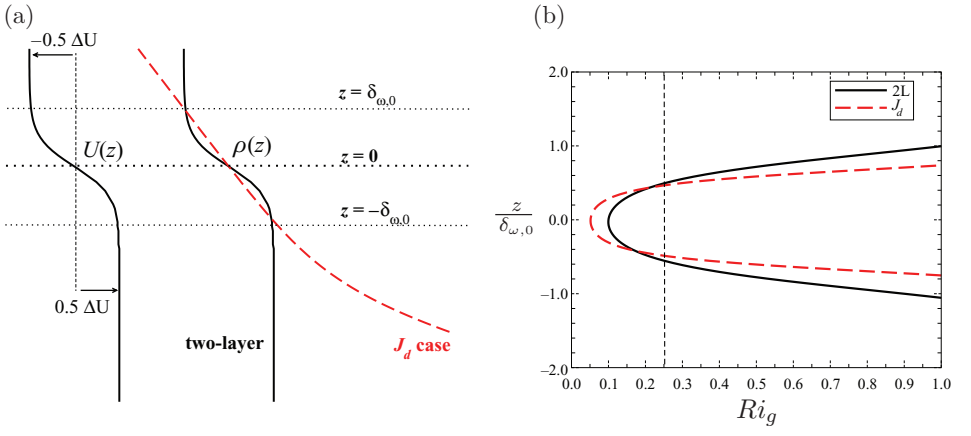

Figure 1. (a) Schematics of initial mean velocity and density profiles, (b) initial gradient Richardson number Ri_g. The dashed line indicates the marginal value, Ri_g=0.25, for shear instability.

$\Delta\rho_0^*$, across $2\delta_{\omega,0}$ is the same for both cases and J_d is equal to $5J_s$. The initial velocity and density profiles are shown in Figure 1(a). The two-layer profile has been studied previously [7, 9, 11, 12] and the corresponding mixing efficiency has been discussed at length [13] and will be used as a base case for comparison in the current study. The J_d profile is typical to numerous observations in the ocean pycnocline as well as in the atmospheric inversion in which the background density stratification varies with depth/height.

The governing equations are the incompressible Navier–Stokes equation with Boussinesq approximation with dependent variables: velocity u, v, w, pressure p and density ρ in a nonrotating Cartesian coordinates with independent variables: x, y, and z. The variable p denotes deviations from the mean hydrostatic pressure. The density is decomposed into a reference density ρ_0 and a departure, which is composed of a mean and fluctuation as follows:

$$\rho = \rho_0 + \langle\rho\rangle(z) + \rho'(x, y, z, t).$$

The apostrophe indicates the fluctuation from the planar mean value. In the current study, fluctuations can represent both waves and turbulence. The Boussinesq approximation supposes that the variations in density are ignored in the inertial terms in the momentum equations but they contribute to the gravitational force. Using $\delta^*_{\omega,0}$, ΔU^*, ρ^*_0, and $\Delta\rho^*_0$ as the characteristic scales for length, velocity, density, and density difference in the momentum equation, respectively, the non-dimensional governing equations take the following form:

$$\nabla\cdot\mathbf{u} = 0, \tag{1}$$

$$\frac{\partial\mathbf{u}}{\partial t} + (\mathbf{u}\cdot\nabla)\mathbf{u} = -\nabla p + \frac{1}{Re_0}\nabla^2\mathbf{u} - Ri_{b,0}\rho'\delta_{i3}, \tag{2}$$

$$\frac{\partial\rho}{\partial t} + (\mathbf{u}\cdot\nabla)\rho = \frac{1}{Re_0 Pr}\nabla^2\rho, \tag{3}$$

where

$$Re_0 = \frac{\Delta U^*\delta^*_{\omega,0}}{\nu^*}, \quad Ri_{b,0} = \frac{g^*\Delta\rho^*_0\delta^*_{\omega,0}}{\rho^*_0\Delta U^{*2}}, \quad Pr = \frac{\nu^*}{\kappa^*}. \tag{4}$$

Downloaded by [University of California, San Diego] at 17:42 17 November 2014

Downloaded by [University of California, San Diego] at 17:42 17 November 2014

Here, ν^* and κ^* are the kinematic viscosity and molecular diffusivity, respectively. Both datasets are generated with $Re = 5000$, $Pr = 1$ and $Ri_{b,0} = 0.1$. It is noted that although the bulk Richardson number $Ri_{b,0}$ are the same, the gradient Richardson number $Ri_g(z) = N^2(z) / (d\langle u \rangle / dz)^2$ at the centerline in the two-layer case is twice larger than that in the J_d case as shown in Figure 1(b).

The initial value of Re is sufficiently large such that the initial instability is nearly inviscid and the separation between the largest and the smallest length scales is approximately three orders of magnitude assuming the separation scales as $Re^{-3/4}$. The initial Ri_b is chosen to be less than the critical value of 0.25 for shear instability [18]. The parameters used in this study are relatively low for environmental applications. Nonetheless, Smyth et al. [13] has simulated a 3D-DNS of a mixing layer with the two-layer profile with $Re = 4978$, $Pr = 1$, and $Ri_b = 0.08$, and compared the computed mixing efficiency to the values from measurements in turbulent patches observed off the California coast and at the equator. They concluded that the parameters in their DNS is high enough to approximate a high Re limit and further increase in Re would not significantly alter their DNS results.

The numerical method is similar to that in our previous work [19, 20]. Briefly, a second-order finite difference method on a staggered grid is used for spatial discretization and the simulation is marched in time with third-order low-storage Runge–Kutta schemes. The current DNS utilizes parallel computing with message-passing interface (MPI) to handle the computational needs of simulating high Re flows. The domain size is $30.75 \times 15.39 \times 93.6$ and the grid has $1024 \times 512 \times 768$ points in the x, y, and z directions, respectively, for a total of 402 million gridpoints. The domain length L_x is chosen to accomodate approximately four wavelengths of the primary K–H instability. The grid is uniform in the streamwise (x) and spanwise (y) directions with a spacing of 0.03. In the vertical direction, the grid is uniform in the region $-4.5 < z < 3$ with a spacing of 0.03, while the grid is stretched at the rate of 1% outside. Low-amplitude velocity perturbations with a broadband spectrum,

$$E(k)\,\alpha\left(\frac{k}{k_0}\right)^4 exp\left[-2\left(\frac{k}{k_0}\right)^2\right],$$

are added to initialize the flow. Here, k_0 is set such that the spectrum peaks at 1.7. Fluctuations are introduced only in the shear layer with the shape function,

$$A(z) = exp(-z^2).$$

and with a maximum amplitude of 1% ΔU.

Periodic boundary conditions are used in the streamwise and spanwise directions. In the J_d case, the top and bottom faces of the domain have the following conditions:

$$\begin{aligned} u(z_{min}) &= \frac{1}{2}, \quad u(z_{max}) = -\frac{1}{2}, \\ v(z_{min}) &= v(z_{max}) = 0, \\ p(z_{min}) &= p(z_{max}) = 0, \\ \frac{\partial w}{\partial z}(z_{min}) &= \frac{\partial w}{\partial z}(z_{max}) = 0, \end{aligned}$$

$$\frac{\partial \rho}{\partial z}(z_{max}) = \frac{-J_s}{Ri_{b,0}},$$
$$\frac{\partial \rho}{\partial z}(z_{min}) = \frac{-J_d}{Ri_{b,0}}.$$

In the two-layer case, the velocity boundary conditions are the same but the density ρ has a no-flux condition. As internal waves can propagate far away from the shear layer, a sponge region is added at the top ($z > 15$) and the bottom ($z < -50$) boundaries to control spurious reflections of internal waves. More details about the numerical methods can be found in [17, 19, 20].

3. Evolution of the shear layers

The evolution of the shear layer, which consists of shear instability, formation of K–H rollers, their breakdown into 3D turbulence, and finally the decay of turbulence can be described with the growth of the momemtum thickness δ_θ defined as

$$\delta_\theta = \int_{z_l}^{z_u} \left(\frac{1}{4} - \frac{\langle u \rangle^2}{\Delta U^2} \right) dz,$$

where the depths z_u and z_l are taken to be 5 and -5, respectively. The depths are locations at which the background shear $d\langle u \rangle / dz$ is approximately zero over time, although the momentum flux $\langle u'w' \rangle$ due to internal waves can be large. The growth of δ_θ shown in Figure 2(a) indicates three evolutionary regimes for both cases. During the early stage approximately $0 < t < 25$, the shear layer adjusts to the initial conditions and the growth is similar between both cases. The second regime is the shear instability regime in which the instability develops into the K–H rollers and the shear layers thicken at strong linear rate. The linear growth rate is similar between the two cases, although it starts and ends earlier in the J_d case. As a result, δ_θ in the J_d case is significantly smaller at end of the second regime when the K–H rollers can no longer grow and small-scale turbulence dominates the shear layer. The transition from the second regime to the third regime in which the shear

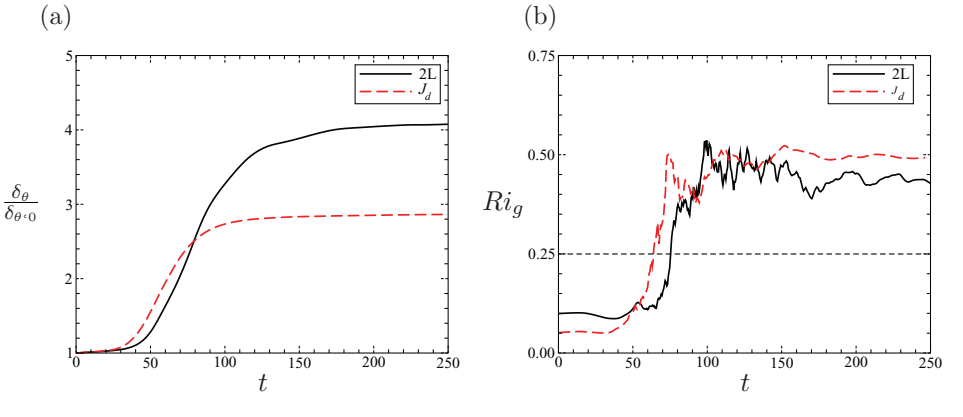

Figure 2. Evolution of (a) the momentum thickness δ_θ, and (b) the gradient Richardson number Ri_g at the centerline of the shear layer z=0. The dash line indicates the critical value of Ri_g=0.25 for shear instability.

Downloaded by [University of California, San Diego] at 17:42 17 November 2014

Downloaded by [University of California, San Diego] at 17:42 17 November 2014

layer is dominated by decay of turbulence is sharper in the J_d case. In the two-layer case, during the transition the turbulent shear layer thickens although at significantly smaller rate compared to the growth observed in the second regime. In the third regime as the turbulence decays, the growth of δ_θ becomes asymptotic at a value which is more than 25% larger in the two-layer case.

The evolution of Ri_g computed at the center of the shear layer $z = 0$ is shown in Figure 2(b). In both cases, Ri_g grows at similar rate during the formation of the K–H rollers and exhibits strong fluctuations during the transition to turbulence. After that Ri_g asymptotes to a constant value. Although the initial value of Ri_g is half of that in the two-layer case, the value during the turbulence decaying stage is larger in the J_d case. The asymptotic value is approximately 0.45 in the two-layer case and 0.5 in the J_d case.

4. Turbulence evolution

In the previous section we have described the evolution of the mean flow. In this section we focus on the evolution of turbulence in the shear zone which consists of two stages: the generation of turbulence through shear instability and the decay of turbulence through molecular mixing and spatial transport to the ambient. Although the stages are the same between the two cases, there are differences which affect the turbulent mixing rate. We elaborate on the differences with the visualization of the shear layer, the TKE budget, the budget of density variance, and the evolution of relevant length scales, as well as some non-dimensional turbulence parameters.

4.1. *Visualization of the turbulent fields*

Cross sections of the density fields in the simulated flows are shown in Figure 3. Figures 3(a–c) correspond to the two-layer case, while Figures 3(d–f) correspond to the J_d

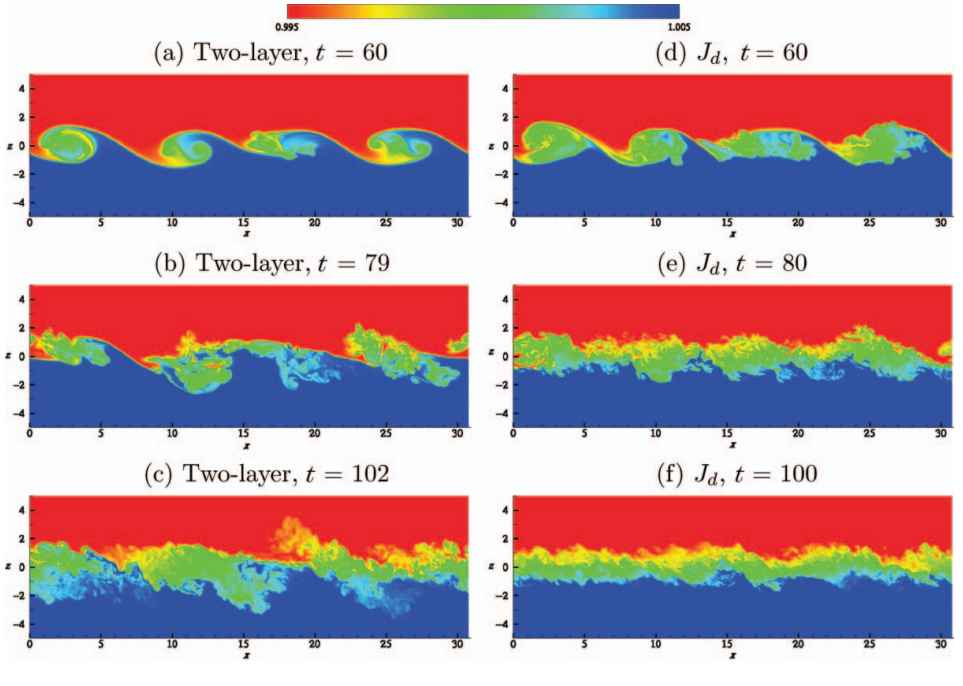

Figure 3. Density field on a vertical xz plane at $y = 3.9$.

Downloaded by [University of California, San Diego] at 17:42 17 November 2014

case. In both cases, the primary shear instability is the same as shown in Figures 3(a and d) with the horizontal domain consisting of four K–H rollers. The vertical extent of the largest rollers, located at the far left, is also similar. The pairing of K–H rollers is absent in both cases. The presence/absence of pairing influences the evolution of the vertical length scales, which consequently affects the amount of potential energy available for mixing. In the two-layer case, the two rollers to the right are breaking in Figure 3(a). Four isolated patches of small-scale turbulence in Figure 3(b) corresponding to the four rollers in Figure 3(a) indicate evidence of breaking without pairing. The braid between the first roller and the second roller, as well as one between the third roller and the fourth roller in Figure 3(b) are still coherent even though the cores of the rollers show significant disintegration. In the J_d case, all four rollers in Figure 3(d) exhibit high-frequency fluctuations in the roller cores. Figure 3(e) shows the shear layer at $t = 80$, which already consists of small-scale turbulence. Pham et al. [17] observed pairing in the two-layer case but not in the J_d case. Their physical explanation is that, in the J_d case, strong internal waves carry a significant amount of energy outside the shear layer and thus the rollers in the shear layer become too weak to pair. In the current study in which the *Re* is approximately four times larger, low viscosity allows for small-scale growth; therefore, the K–H rollers, even in the two-layer case, tend to break down before they can pair. At approximately $t = 102$, the turbulence in the shear layer in the two-layer case shown in Figure 3(c) becomes more homogenous in the horizontal extent compared to that in Figure 3(b). The braids between the turbulent patches in Figure 3(b) can no longer be identified in Figure 3(c). In the J_d case, at $t = 100$, the turbulence in the shear layer in Figure 3(f) is already decaying. Comparison of the shear layer in Figure 3(e) to that in Figure 3(f) shows that the former has stronger fluctuations and larger vertical extent. Between the two cases, the turbulence in the two-layer case in Figure 3(c) spreads to a greater vertical extent than that in the J_d case in Figure 3(e).

Figure 4 illustrates the TKE dissipation field, $\varepsilon = (2/Re_0)\langle s'_{ij}s'_{ij}\rangle$, where s'_{ij} is the fluctuating strain rate, corresponding to the density fields shown in Figure 3. Here the fluctuations from the planar mean can represent both internal waves and turbulence, although the latter has broader energy spectra and larger dissipation rate [17]. During the generation period of the K–H rollers, intense dissipation occurs in the braid regions, where the strain is large. As the flows transition into turbulence, small-scale fluctuations raise the dissipation rate inside the roller cores as in Figure 4(b and d). The breaking rollers transform into localized patches of dissipation. In Figures 4(c and e) the shear layers are fully turbulent. The dissipation patches observed at earlier time merge with each other. The fluctuations at the center of the shear layers become homogeneous in the horizontal extent in Figures 4 (c,e, and f).

Figure 5 shows the dissipation rate, $\chi_\rho = 2/(Re_0 Pr)\langle(\partial\rho'/\partial x_i)^2\rangle$, of the density variance. This quantity is related to the rate at which the turbulent potential energy is lost. An inverse correlation between the spatial distribution of the χ_ρ and ε fields of the K–H rollers is observed when comparing Figures 5(a and d) to Figures 4(a and d). The K–H roller at the far left in Figure 5(a) has χ_ρ small in the core and large in the envelope. In constrast, Figure 4(a) shows ε large in the core and small in the envelope. The observation is consistent with the fact that the envelope has larger instantaneous density gradient and thus larger χ_ρ. Similar behavior is observed when the shear layer becomes turbulent. While ε is usually not large at the edges, Figures 4 (e and f), χ_ρ is large at the edges of the shear layer as in Figures 5(e and f). Evidence of internal waves is seen in Figures 5(d,e, and f). The wave phase lines have mild χ_ρ, only a magnitude of order larger than the backgound value.

In addition to the primary K–H instability in the spanwise direction, we also observe the secondary instability in the streamwise direction that has been discussed previously by

Downloaded by [University of California, San Diego] at 17:42 17 November 2014

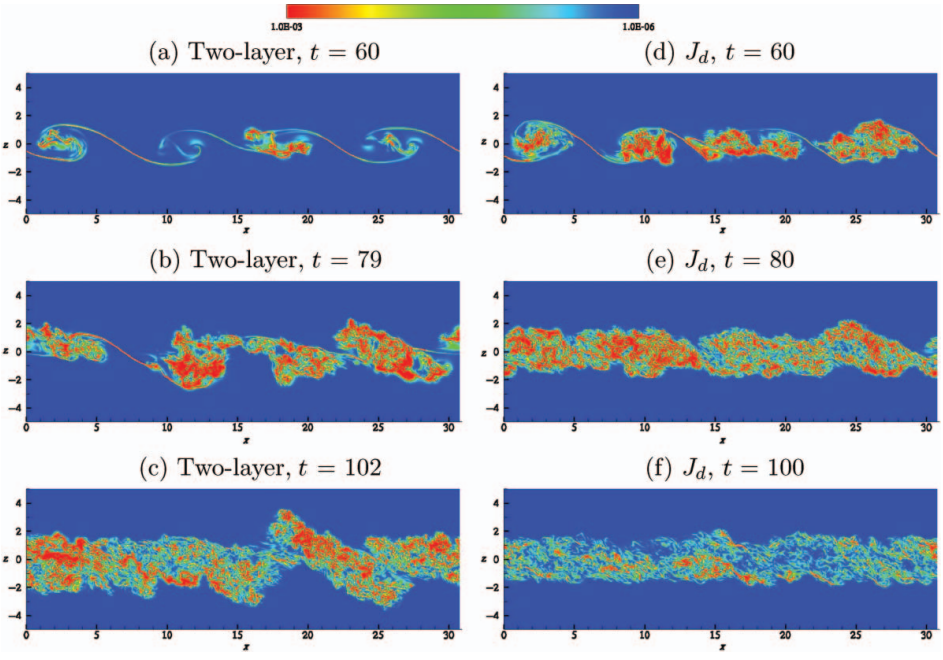

Figure 4. TKE dissipation rate ε on a vertical xz plane at $y = 3.9$.

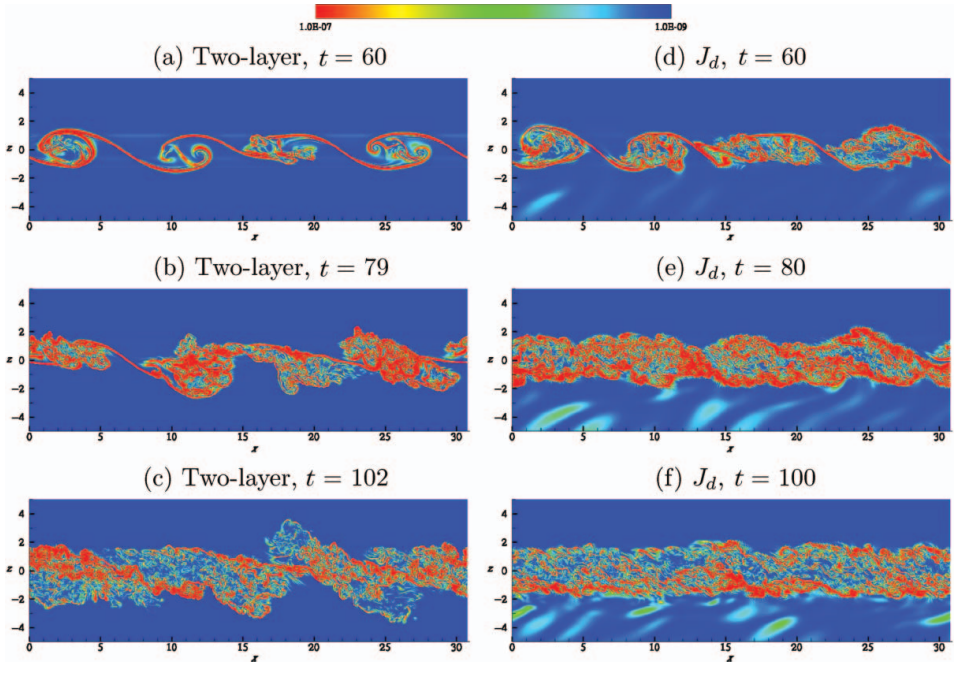

Figure 5. Density variance dissipation rate χ_ρ on a vertical xz plane at $y = 3.9$.

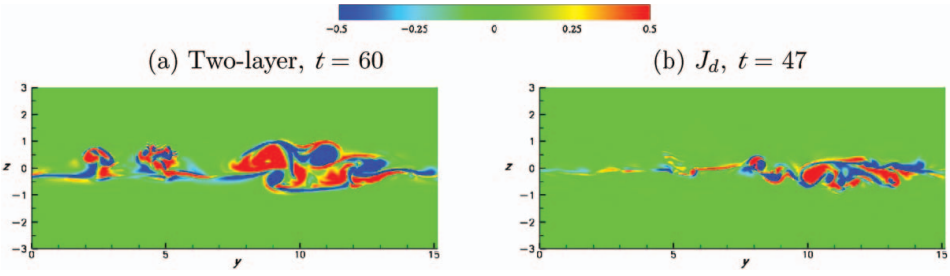

Figure 6. Streamwise vorticity ω_1 on a vertical tranverse plane at $x = 15.4$.

[7]. Figures 6(a and b) show the field of streamwise vorticity ω_1 on the yz cross section at $x = 15.4$. The cross section is a cut through the braid region shown in Figure 3. In the two-layer case, shown in Figure 6(a), the braid consists of vortex streaks. The secondary instability is observed at four different y locations on the braid. A pair of counter-rotating vortices pinches off the braid at $y \approx 2.5$, while at $y \approx 5$ a group of smaller vortices are observed. At $y \approx 10$, a larger pair of counter-rotating vortices floats upward, while a smaller pair cleaves off in the opposite direction. Another vortex pair is at $y \approx 12$.

In the J_d case, shown in Figure 6(b), the instability is observed at $y \approx 8$, 9 and 10. The pair at $y \approx 8$ floats upward, the pair at $y \approx 9$ sinks downwards, and the pair at $y \approx 10$ is the largest. A group of incoherent vortices are observed in the region $11 < y < 14$. The instability in the current study is not as coherent as shown in the study of Werne et al. [8] because the initial fluctuations employed here have broandband spectrum in contrast to the flow initialization with primary K–H instability [8], which subsequently triggers the secondary instability. Caulfield and Peltier [7] suggest that the secondary instability triggers 3D perturbations which transition the flow from a 2D quasi-laminar state to 3D turbulence. In other words, turbulence is initiated from the braids of the K–H rollers, spreads toward the core, and causes the breakdown of the rollers in the earlier low-Re DNS. In the current study, due to the high Re and broadband nature of the initial low-amplitude fluctuations, we observe that the generation of turbulence at the braid and at the core of the rollers is independent. Figure 4(b) shows the braid at $x \approx 7$ is still coherent, while the cores of the rollers to the left and right of the braid already contain 3D fluctuations.

The properties of the internal wave field generated by an unstable shear layer has been discussed at length by Pham et al. [17]. Here, we provide a short discussion of the internal wave field for completeness and also because Re is approximately four times larger in the current simulations. Figure 7(a) shows the anatomy of the wave field with the cross section of the fluctuating vertical velocity w' field, while Figure 7(b) shows the internal wave flux to be discussed later. The narrow-band waves are linear with the horizontal wavelength equal to the wavelength of the K–H rollers in the shear layer. The wave phase lines tilt downward and upstream at any angle between 32° and 38° to the vertical. The direction of propagation can be explained using linear wave theory based on the Doppler-shifted frequency of the K–H mode [17]. With an increase in Re, we do not observe a change in the mechanism of wave excitation.

4.2. *Turbulence Budgets*

The TKE budget for the simulated flows is described by the following equation:

$$\frac{dK}{dt} = P - \varepsilon + B - \frac{dT_3}{dz}\,, \tag{5}$$

Downloaded by [University of California, San Diego] at 17:42 17 November 2014

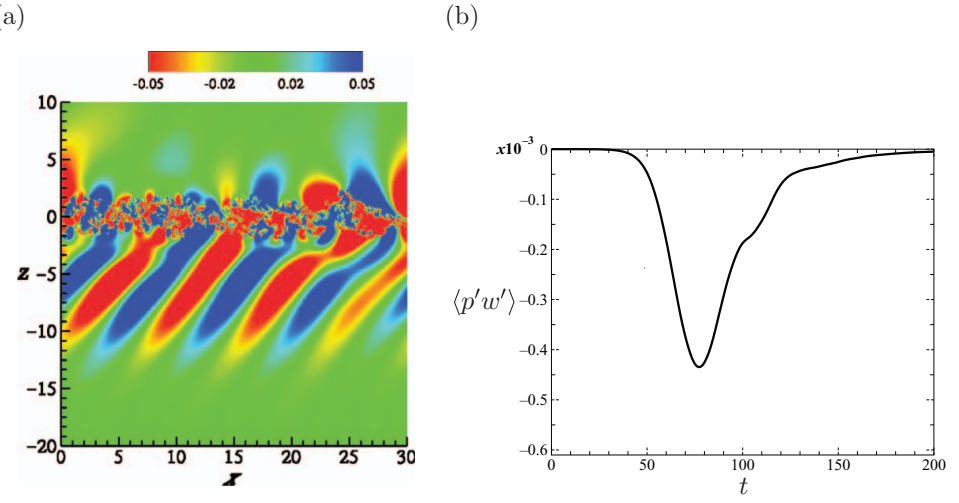

Figure 7. J_d cases: (a) Internal wave field shown in the xz cross section at $y = 3.9$ of the fluctuating vertical velocity w' field at $t = 80$, (b) wave energy flux $\langle p'w' \rangle$ across the horizontal plane $z = -5$.

where, $K = 1/2\langle u_i' u_i' \rangle$ is the TKE. P is the production rate, defined as

$$P = -\langle u'w' \rangle \frac{d\langle u \rangle}{dz},$$

ε is the previously defined dissipation rate, and B is the buoyancy flux, defined as

$$B = -Ri_{b,0} \langle \rho' w' \rangle.$$

The transport term dT_3/dz is defined as

$$T_3 = \frac{1}{2}\left[\langle w'u'u' \rangle + \langle w'v'v' \rangle + \langle w'w'w' \rangle\right] + \frac{\langle p'w' \rangle}{\rho_0} - \frac{2}{Re_0}\left[\langle u's_{31}' \rangle + \langle v's_{32}' \rangle + \langle w's_{33}' \rangle\right].$$

Figures 8(a and b) show the budgets for the two-layer case at $t = 102$ and J_d case at $t = 100$, respectively. At this time, the shear layers are fully turbulent. In both cases, the budgets in the shear layer show the dominant balance between the dissipation ε and production P. In the two-layer case, the buoyancy flux is positive in the upper half of the shear layer and negative in the lower half, indicating B can be both a source and a sink of energy. In the J_d case, B is the source of energy across the shear layer and the profiles of the buoyancy flux B, the transport $-dT_3/dz$ and the transient term dK/dt extend far into the region below the shear layer where internal waves are present. For the wave field, the production and dissipation are insignificant. Total energy transported by the wave fields is balanced by the rate of change of TKE in time and the rate at which TKE is converted to potential energy, i.e. buoyancy flux B.

Downloaded by [University of California, San Diego] at 17:42 17 November 2014

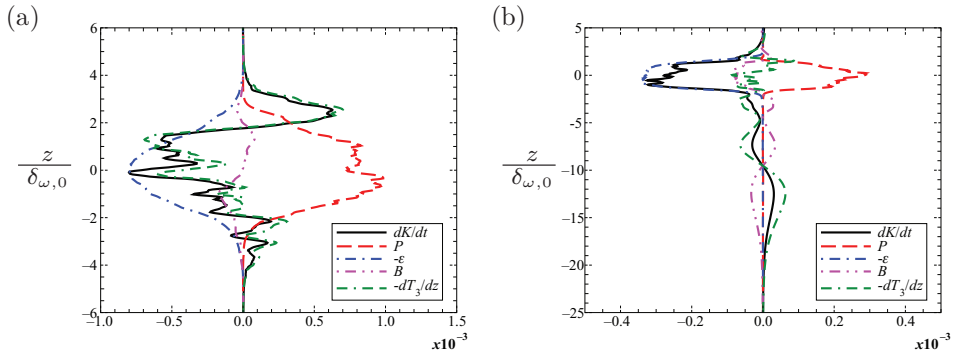

Figure 8. TKE budgets in the vertical direction z: (a) in the two-layer case at $t = 102$, and (b) in the J_d case at $t = 100$.

The wave field in the current study is compared to one reported in Pham et al. [17] in term of energetics. The wave energy flux $\langle p'w' \rangle$ across the horizontal plane $z = -5$ was shown earlier in Figure 7(b). The peak energy flux at $t \approx 75$ is half of the value reported in the previous study. Integrating the energy budget, i.e. equation 5, from $z = -5$ to the upper bound of the domain excluding the sponge region and also in time yields the bulk energy partitions in the balance of integrated TKE. The total wave energy flux is found to be approximately 9% of the integrated production, 17% of the integrated dissipation, and 38% of the integrated buoyancy flux. Pham et al. [17] report values of 17%, 33%, and 75%, respectively. The wave field in the current study is weaker owing to the effects of high Re upon the source region of the waves. At high Re, the energy balance in the TKE budget is in favor of the dissipation over the transport. The energy at the large-scale (K–H mode) cascades into the smaller scales at a faster rate. The K–H rollers at high Re lose more energy to small-scale motion and, therefore, the amount of energy available to excite internal waves is reduced.

Figures 9(a,b) show the time evolution of the production, the dissipation and the buoyancy fluxes at the center of the shear layer $z = 0$ in the two-layer case and the J_d case, respectively. Overall, the evolution starts earlier and ends earlier in the J_d case, while the evolution has a longer duration in the two-layer case. The production rate peaks earlier in the J_d case, although the peak values are comparable between the two cases. Integrated

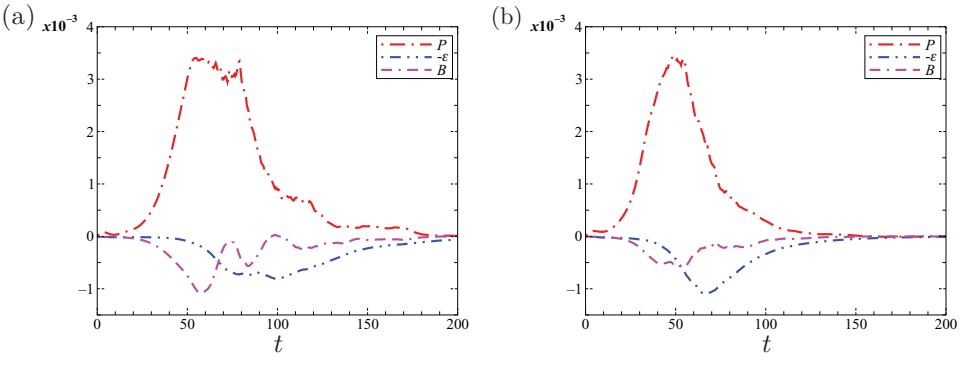

Figure 9. Evolution of TKE production, dissipation, and buoyancy flux measured at center of the shear layer $z = 0$ in time: (a) in the two-layer case, (b) in the J_d case.

Downloaded by [University of California, San Diego] at 17:42 17 November 2014

Downloaded by [University of California, San Diego] at 17:42 17 November 2014

over time, the net TKE production is larger in the two-layer case despite the initial gradient Richardson Ri_g being twice as large. Thus, the production and Ri_g do not have direct correlation; rather, the spatial transport of the Reynolds stress $\langle u'w' \rangle$ plays an important role in quantifying the rate at which TKE is generated. The peak buoyancy flux B has a larger value so that more TKE is transfered to potential energy in the two-layer case. At $t = 100$, B changes signs in Figure 9(a) indicating that available potential energy is converted back to TKE. Different from B, the peak dissipation rate ε is larger in the J_d case. In both cases, B is larger than ε during the rise of P but smaller during the decay of P. After approximately $t = 100$ in the two-layer case and $t = 80$ in the J_d case, the TKE budget shows a balance mainly between P and ε. The effect of the buoyancy flux is small suggesting that the decaying turbulence at the center of the shear layer is in a homogenous state.

The equation for the budget of the density variance $\langle \rho'^2 \rangle$ is

$$\frac{d}{dt}\langle \rho'^2 \rangle = P_\rho - \chi_\rho - \frac{dT_\rho}{dz}, \tag{6}$$

where the scalar production P_ρ is defined as

$$P_\rho = -2\langle \rho' w' \rangle d\langle \rho \rangle / dz \ ,$$

and the scalar dissipation χ_ρ is defined as

$$\chi_\rho = (2/PrRe_0)\,\langle \left(\partial \rho' / \partial x_i\right)^2 \rangle \ .$$

The transport term is

$$\frac{dT_\rho}{dz} = \frac{\partial \langle \rho'^2 w' \rangle}{\partial z} - \frac{1}{PrRe_0}\frac{\partial^2 \langle \rho'^2 \rangle}{\partial z^2}.$$

Figures 10(a,b) show the vertical profiles of the terms in the density variance budgets corresponding to the TKE budgets shown in Figure 8. In both cases, the dissipation inside

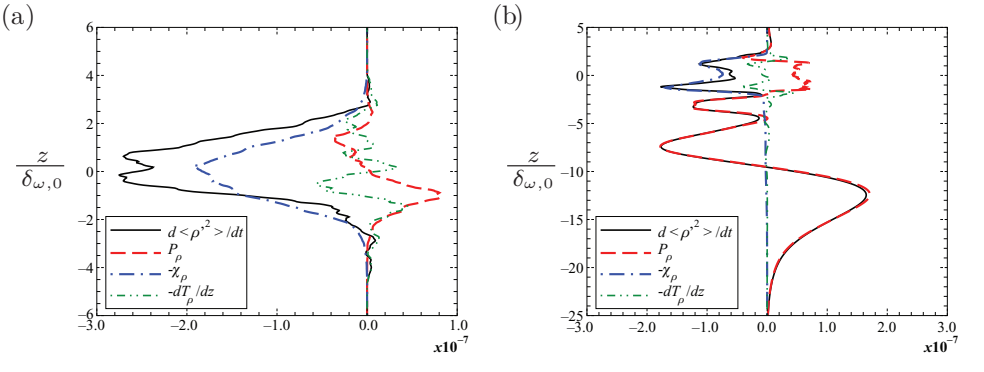

Figure 10. Density variance budgets in the vertical direction z: (a) in the two-layer case at $t = 102$, and (b) in the J_d case at $t = 100$.

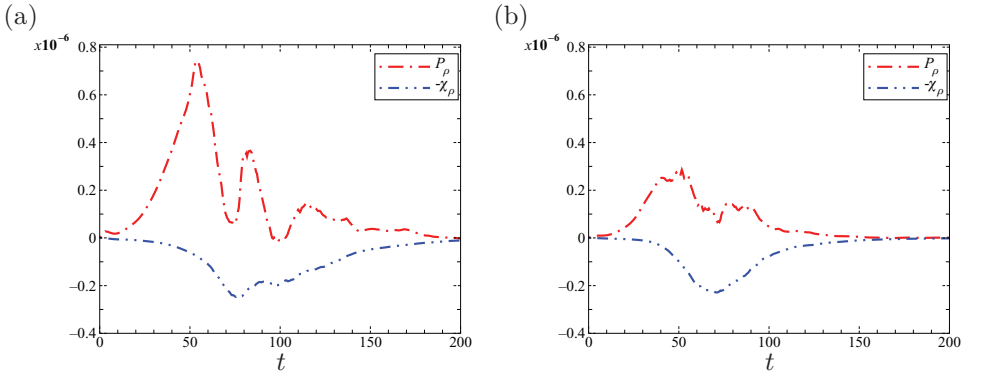

Figure 11. Evolution of production and dissipation of density variance measured at center of the shear layer $z = 0$ in time: (a) in the two-layer case, (b) in the J_d case.

the shear layer is mainly balanced by the transient term indicating the shear layers are in a state of decaying stratified turbulence. In the two-layer case, all terms in the region $z < -3\delta_{\omega,0}$ are zero. In contrast, there is significant buoyancy flux up to $z = -15\delta_{\omega,0}$ in the J_d case, albeit without mixing ($\chi_\rho \simeq 0$). The sign of the production P_ρ and the sign of B shown in Figure 8(a) are opposite; recall that $P_\rho = 2B/Ri_{b,0}d\langle\rho\rangle/dz$ and the stable density gradient has a negative sign. Therefore, B and P_ρ represent energy transfer between the TKE budget and the density variance budget. In the J_d case the production is balanced by the transient term in the region below the shear layer where internal waves propagate. The time evolution of P_ρ and χ_ρ at $z = 0$ for the two-layer and J_d cases are shown in figures 11(a,b), respectively. The peak value of P_ρ is significantly larger in the two-layer case, while the peak value for χ_ρ is the same for the two cases.

4.3. *Length scales*

The growth of the following length scales are now discussed: energy-containing scale L_{EN}, Ellison scale L_E, Ozmidov scale L_O, and Kolmogorov scale L_K. Their definitions [11–13] are given as follows,

$$L_{EN} = \frac{\left(\frac{2}{3}k\right)^{3/2}}{\varepsilon},$$

$$L_E = \frac{\rho_{rms}}{d\langle\rho\rangle/dz},$$

$$L_0 = \left(\frac{\varepsilon}{N^3}\right)^{1/2},$$

$$L_K = \left(\frac{\nu^3}{\varepsilon}\right)^{1/4}.$$

The evolution of these length scales is shown in Figures 12(a and b) for the two-layer case and J_d case, respectively.

The energy-containing scale L_{EN} is calculated using the TKE and the dissipation rate. In both cases, L_{EN} peaks early corresponding to the moment when the K–H rollers reach

Downloaded by [University of California, San Diego] at 17:42 17 November 2014

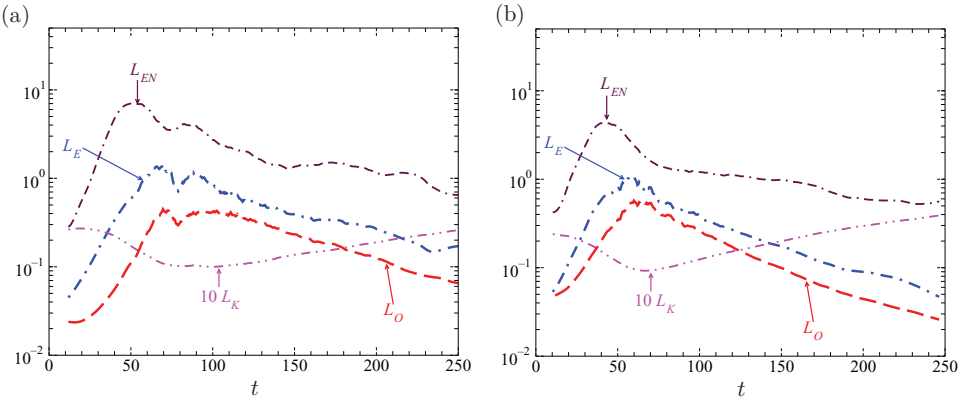

Figure 12. Evolution of length scales: (a) in the two-layer case, and (b) in the J_d case.

their largest size. At this time, the TKE reaches its peak while the dissipation has not yet evolved. The two-layer case has larger peak value of L_{EN} because the K–H rollers are larger. As rollers break and the shear layer turns turbulent, L_{EN} decreases corresponding to an increase in dissipation as shown in Figure 9. At later time when turbulence decays L_{EN} is approximately equal to 1.

In both cases, the evolution of the Ellison scale L_E and Ozmidov scale L_O are similar despite a difference in the magnitude. These two length scales grow and decay similarly and also peak at the same time. The decay is exponential in time. The decay rate in the J_d case is larger than that in the two-layer case. The minimum value for the Kolmogorov scale L_K is nearly equal between the two cases. The value is approximately 0.01, which is a third of the grid spacing. The time at which L_O decreases to the value of 10η marks the buoyant-inertial-viscous (BIV) transition, after which the inertial and buoyancy effects are damped out so that the fluctuations decay mainly due to viscosity. The transition occurs early in the J_d case at $t = 120$ and later in the two-layer case at $t = 180$. The time period of active turbulence indicated by $L_O > 10L_K$ is shorter in the J_d case, $35 < t < 120$, than that in the two-layer case, $55 < t < 180$.

4.4. *Non-dimensional turbulent parameters*

The evolution of the buoyancy Reynolds number $Re_b = \epsilon/(\nu N^2)$, an indicator of turbulent activity, at the center of the shear layer is shown in Figure 13(a) for the two simulated cases. During the period of the formation of the K–H rollers, Re_b is larger in the J_d case although the growth rate of Re_b is the same between the two cases. The peak value of Re_b in the J_d case is approximately twice that in the two-layer case. The larger Re_b is due to smaller value of the squared buoyancy frequency N^2, recalling that the initial Ri_g at the center of the shear layer is twice smaller in the J_d case as shown in Figure 1(b). According to the criterion by which Shih et al. [6] differentiate the mixing regimes, both of our simulations span all three regimes. The time period during which energetic mixing occurs, $Re_b > 100$, is longer in the two-layer case. Note that, as $Re_b = (L_O/L_K)^{\wedge}(4/3)$, the condition $Re_b > 100$ is equivalent to $L_0/L_K > 31$. The decay rate is the same for the intermediate mixing regime and the diffusive regime in both cases.

An alternative measure of turbulent activity is $Re_T = qL_E/\nu$, where $q = \sqrt{2k}$ [6]. Different from Re_b where information at the small scale, i.e. dissipation rate ε, is required,

Downloaded by [University of California, San Diego] at 17:42 17 November 2014

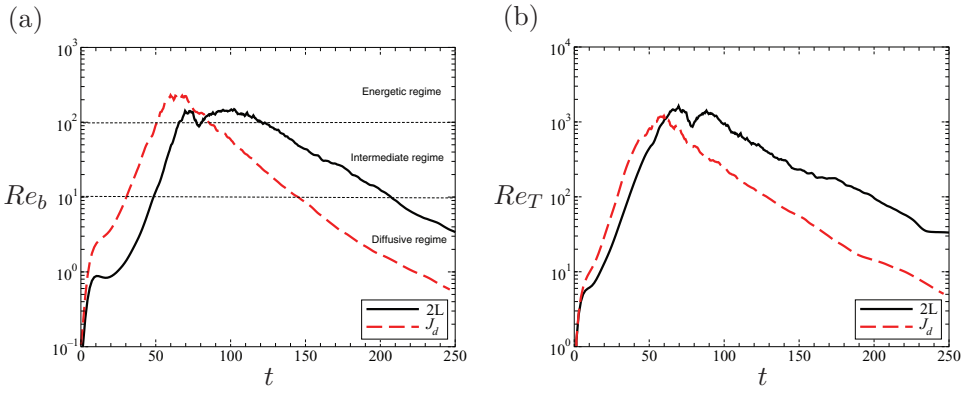

Figure 13. Evolution of (a) buoyancy Reynolds number, $Re_b = \epsilon/(\nu N^2)$, and (b) local turbulent Reynolds number $Re_T = qL_E/\nu$. Both are at the shear center.

Re_T can be estimated using only information at the large scale, thus Re_T is more convenient to modellers. L_E is prefered to L_O despite their similar evolution because L_0 involves the dissipation rate in its definition. Figure 13(b) shows the evolution of Re_T, qualitatively captures the shape of the evolution of Re_b in Figure 13(a) in both cases. The magnitude and the decay rate show some differences. The peak value of Re_T is an order of magnitude larger than the peak value of Re_b. Also, the peak value of Re_T is larger in the two-layer case; the opposite is observed in Re_b. The decay rate of Re_T is smaller than that of Re_b. During the intermediate mixing regime, the exponential decay rate for Re_b is -0.027 in the two-layer case and -0.039 in the J_d case. For Re_T, the values in the two cases are -0.02 and -0.03, respectively.

5. Eddy diffusivity and its parameterization

The eddy diffusivity is defined as

$$K_\rho = \frac{-\langle \rho' w' \rangle}{d\langle \rho \rangle / dz} = \frac{-B}{N^2}. \tag{7}$$

K_ρ is a 'reversible' estimate since B can be both positive and negative in the evolution of the TKE budget. The evolution of K_ρ is shown in Figure 14(a). Overall, K_ρ is significantly larger during the period of K–H roller formation compared to later time when there is broadband turbulence. The increase of K_ρ in the J_d case begins earlier but K_ρ has larger peak values in the two-layer case. K_ρ has negative value at $t = 100$ in the two-layer case.

The buoyancy Reynolds number, $Re_b = \varepsilon/(\nu N^2)$, has been used for parameterization in ocean turbulence, where ε is obtained from microstructure profilers and the momentum diffusivity K_ρ is inferred from ε. In particular, a mixing efficiency defined as $\Gamma = -B/\varepsilon$ is introduced into the last equality of Equation (7) to give

$$K_\rho = \Gamma \frac{\varepsilon}{N^2}, \tag{8}$$

which can be be alternatively written as

$$\frac{K_\rho}{\kappa} = \Gamma Pr \frac{\varepsilon}{\nu N^2} = \Gamma Pr Re_b. \tag{9}$$

Downloaded by [University of California, San Diego] at 17:42 17 November 2014

Downloaded by [University of California, San Diego] at 17:42 17 November 2014

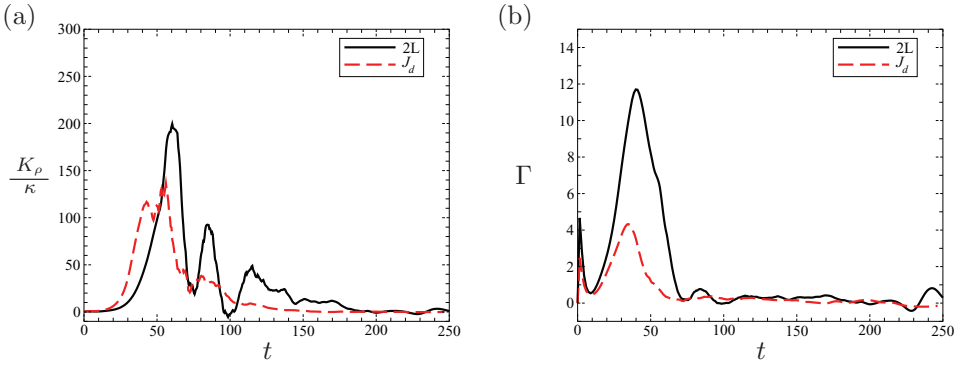

Figure 14. Evolution of (a) eddy diffusivity K_ρ, and (b) mixing efficiency Γ at the center of the shear layer.

Choice of a value for Γ, often taken to be $\Gamma = 0.2$, completes the parameterization of K_ρ. Note that Equation 9 implies a physically consistent behavior that the eddy diffusivity in stratified turbulence increases with both decreasing stratification and increasing turbulent dissipation rate. Figure 14 shows the evolution of Γ. In both cases, Γ is much larger than 0.2 when the rollers are forming but it reduces to become approximately constant during the turbulence decay.

We now examine how K_ρ varies with respect to Re_b. The variation is shown in Figure 15(a), and the mixing regimes shown in the figure are determined by the criteria of Shih et al. [6]. The arrows indicate the time progression in which the simulations proceed. The direct one-to-one relationship that was seen previously in decaying stratified homogenous turbulence [6] is not seen here; rather, the evolution of K_ρ exhibits four distinct stages. The first is the generation stage, $1 < Re_b < 50$ for both cases, during which K_ρ grows with approximately linear dependence on Re_b corresponding to the formation of the K–H rollers. K_ρ is twice that in the two-layer case at the end of this stage. The second stage is the transition to turbulence, $50 < Re_b < 90$ in the two-layer case and $50 < Re_b < 200$ in the J_d case, during which K_ρ is approximately constant. The third is the collapse stage during which Re_b (equivalently turbulence dissipation rate) cannot grow further and K_ρ

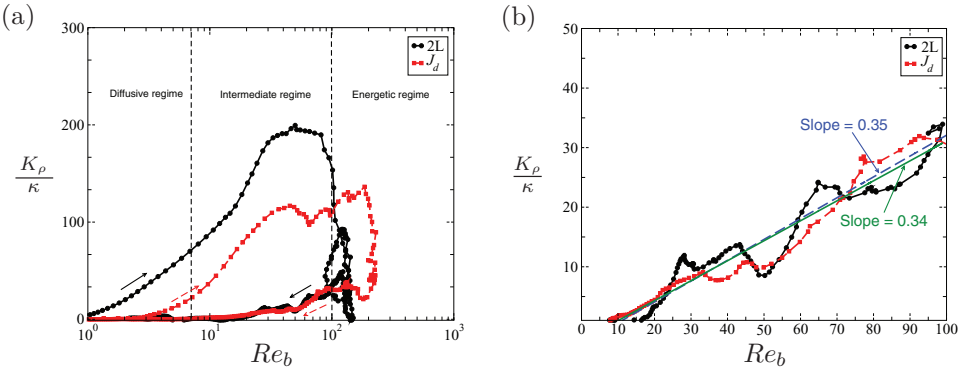

Figure 15. (a) $K_\rho vs Re_b$; (b) same as in (a) zoomed on to the intermediate mixing regime during the decay of the flow. Arrows indicate progress in time. Note the abscissa is given in logarithmic scale in (a) and linear scale in (b).

Downloaded by [University of California, San Diego] at 17:42 17 November 2014

exhibits a sharp drop. The collapse is smoother in the J_d case in which K_ρ drops at constant Re_b. In the two-layer case K_ρ rises and falls many times within a small range of Re_b. Finally, the fourth stage corresponds to turbulence decay during which Re_b and K_ρ decreases simultaneously. The evolution of K_ρ in the two cases is similar only during the fourth stage suggesting that turbulence eventually becomes independent of the initial and background flow conditions. It is in this fourth stage that the eddy diffusivity can be directly related to Re_b as was done for uniform shear flow turbulence by [6]. Figure 15(b) shows a zoom on to the intermediate mixing regime. Even though K_ρ shows fluctuations, the best-fit lines are similar between the two cases. Recall that the slope of $K_\rho/(\kappa Re_b)$ with $Pr = 1$ is the mixing efficiency Γ. The slopes of the best-fit lines indicate $\Gamma \approx 0.35$, which is higher than 0.2, the value typically used by the oceanic community.

It is difficult to measure fluctuating gradient statistics accurately and, therefore, there is interest in a more easily measurable alternative to Re_b that can be used to infer K_ρ. The turbulent Reynolds number, Re_T, introduced in the previous section is a measure of turbulence activity. The gradient Richardson number, $Ri = N^2/S^2$, and the turbulent Froude number, $Fr_T = q/(NL)$ are measures of stratification. The Reynolds and Froude numbers can be related to Re_b as follows:

$$Re_b = \frac{\epsilon}{\nu N^2} = \frac{\alpha q^3/L_E}{\nu N^2} = \alpha \frac{qL_E}{\nu}\frac{q^2}{L_E^2 N^2} = \alpha Re_T Fr_T^2, \tag{10}$$

where α is a proportionality coefficient. The Reynolds and gradient Richardson numbers can be related to Re_b from the third equality in Equation (10) as follows:

$$Re_b = \alpha \frac{qL_E}{\nu}\frac{q^2}{L_E^2 N^2} = \alpha \frac{qL_E}{\nu}\frac{S^2}{\beta^2 N^2} = \frac{\alpha}{\beta^2}\frac{Re_T}{Ri_g}, \tag{11}$$

where SL_E/q is another proportionality coefficient. The use of $Re_T Fr_T^2$ has been explored by [21] using DNS of Taylor–Green vortices, while [6] have explored the use of Re_T/Ri_g using DNS of uniform shear flow.

The evolution of K_ρ with respect to Re_T is shown in Figure 16(a). The evolution of K_ρ depicted by Re_T also consists of four stages similar to when Re_b is used. The general

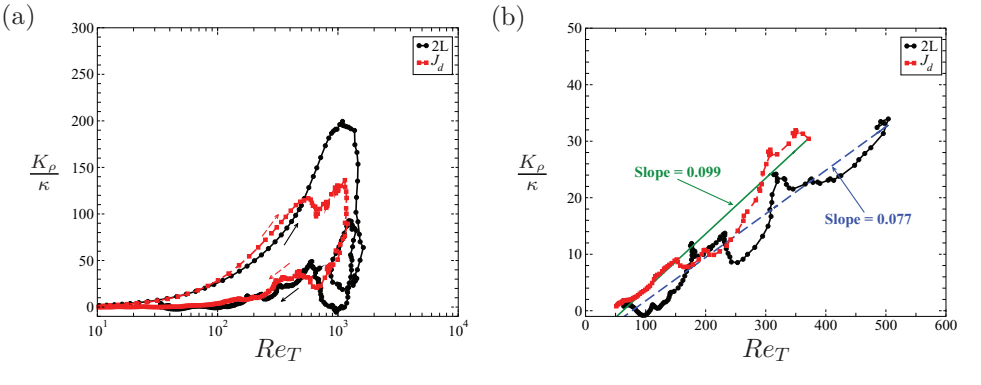

Figure 16. (a) K_ρ vs. Re_T, and (b) same as (a) zoomed on to the intermediate mixing regime during the decay of the flow. Arrows indicate progress in time. Note the abscissa is given in logarithmic scale in (a) and linear scale in (b).

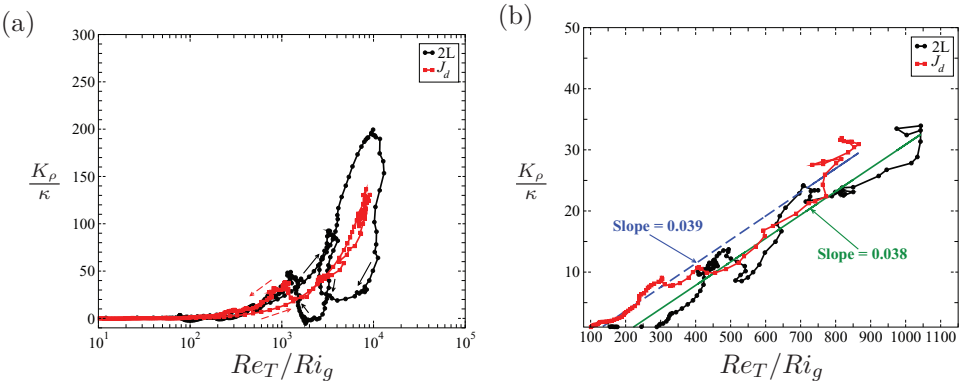

Figure 17. (a) K_ρ vs. Re_T/Ri_g, and (b) same as (a) zoomed on to the intermediate mixing regime during the decay of the flow. Arrows indicate progress in time. Note the abscissa is given in logarithmic scale in (a) and linear scale in (b).

shapes of the evolution in Figures 15(a) and 16(a) in both cases are considerably similar. Both Re_b and Re_T span two-order-of-magnitude range but Re_T is approximately an order of larger magnitude. Compared to Figure 15, Figure 16 shows a smaller difference during the generation stage between the two cases. The collapse stage in the J_d case occurs at larger Re_b but at smaller Re_T relative to the two-layer case. Figure 16(b), a surrogate to Figure 15(b), indicates that the slope during the intermediate mixing regime is 0.077 in the two-layer case and 0.099 in the J_d case when Re_T is used in place of Re_b. The normalized difference in the slopes between the two cases is larger than that computed using Re_b. Overall, Re_T can be used as a qualitative surrogate to Re_b only in terms of depicting the evolutionary processes but parameterizing K_ρ using Re_T is not promising because the dependence of K_ρ on Re_T is not universal, i.e. case-dependent, even during the turbulence decay.

Different from Re_T, the evolution of K_ρ with respect to the ratio Re_T/Ri_g shown in Figure 17(a) is not the same as the one with respect to Re_b in Figure 15(a). Re_T/Ri_g fails to depict the evolution of K_ρ during the generation, transition, and collapse stage, although it does well during the final turbulence decay stage. The expansion of the decay stage in Figure 17(a) is shown in Figure 17(b). The best-fit lines show a slope of 0.038 in the two-layer case and a slope of 0.039 in the J_d case. The difference between the two values is significantly smaller than those computed based on Re_T alone. Consider Re_T/Ri_g is an order of magnitude larger than Re_b, the mixing efficiency computed using $10Re_T/Ri_g$ in place of Re_b is approximately $0.38 - 0.39$ which provides a close agreement with the value of 0.35 shown in Figure 15(b).

6. Eddy diffusivity estimated using irreversible mixing

When the transient and the transport terms in Equation (6) are negligible, the estimated eddy diffusivity can be defined in terms of χ_ρ, the dissipation rate of the density variance, as follows:

$$\tilde{K}_\rho = \frac{\chi_\rho}{2\,(d\langle\rho\rangle/dz)^2}.$$

The evolution of $\tilde{K}_\rho$ shown in Figure 18(a) is similar between the two cases. $\tilde{K}_\rho$ grows exponentially during the K–H roller formation and decays exponentially after the shear

Downloaded by [University of California, San Diego] at 17:42 17 November 2014

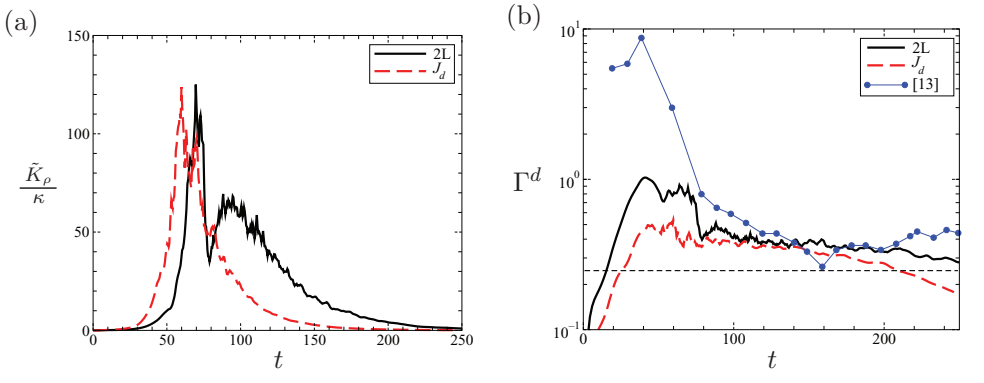

Figure 18. Evolution of (a) estimated eddy diffusivity $\tilde{K}_\rho$, and (b) irreversible mixing efficiency Γ^d. Arrows indicate progress in time. Note the abscissa is given in logarithmic scale in (a) and linear scale in (b).

layer becomes turbulent. Different from K_ρ whose peak value is larger in the two-layer case, the peak values of $\tilde{K}_\rho$ are comparable between the two cases. In the two-layer case, $\tilde{K}_\rho$ increases to its peak value, momentarily decreases at $t = 70$, then increases again before the exponential decay. The secondary growth is absent in the J_d case resulting in smaller $\tilde{K}_\rho$ during the decay. When $\tilde{K}_\rho$ is used in place of K_ρ in the definition of the mixing efficiency $\Gamma = K_\rho \varepsilon / N^2$, the corresponding mixing efficiency is $\Gamma^d = 0.5N^2/(d\langle\rho\rangle/dz)^2\,(\chi_\rho/\varepsilon)$ and its evolution is plotted in Figure 18(b). Overall, Γ^d is larger than 0.2, the value used in the oceanic community. During the time $80 < t < 160$, Γ^d is approximately 0.4, which agrees with the results from the DNS of the two-layer case of Smyth et al. [13] and also with the results of decaying turbulence generated by Taylor–Green vortices of Riley and deBruynKops [5].

Different from the evolution of K_ρ with respect to Re_b, where four distinct stages are observed, the evolution of $\tilde{K}_\rho$ with respect to Re_b shown in Figure 19(a) consists of only two stages: generation and decay. In the J_d case, the two stages lay on top of each other. In the two-layer case, there is an offset in Re_b between the two stages. The decay stage of the two-layer case also coincides with that of the J_d case. The difference in the generation

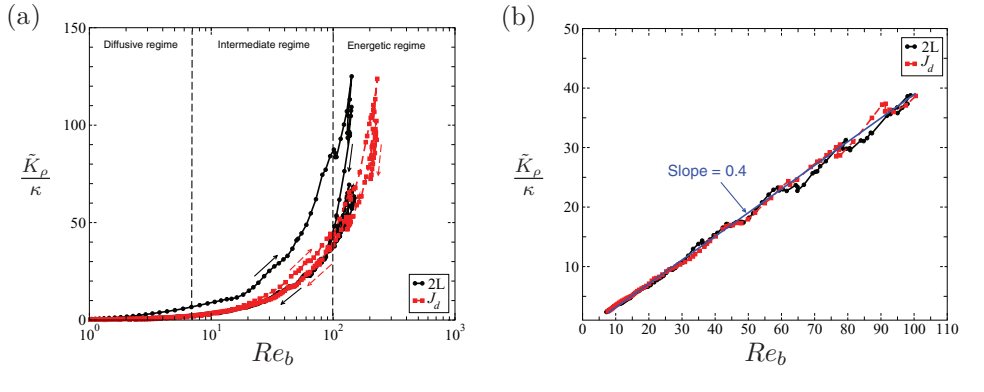

Figure 19. (a) $\tilde{K}_\rho$ vs. Re_b, and (b) same as (a) zoomed on to the intermediate mixing regime during the decay of the flow. Arrows indicate progress in time. Note the abscissa is given in logarithmic scale in (a) and linear scale in (b).

Downloaded by [University of California, San Diego] at 17:42 17 November 2014

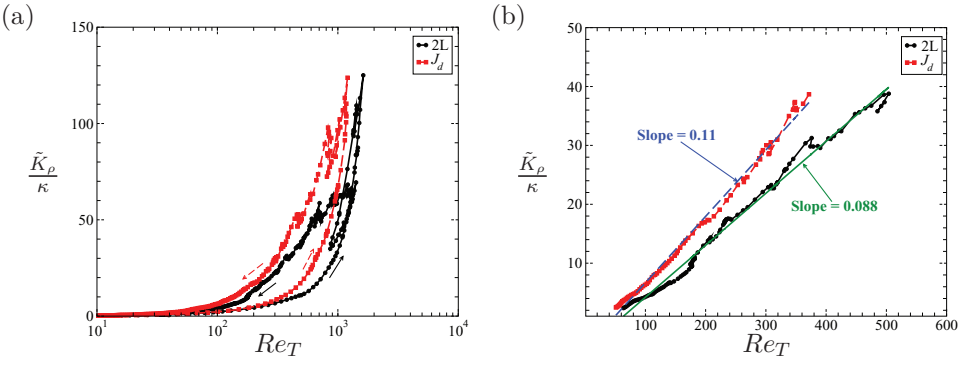

Figure 20. (a) $\tilde{K}_\rho$ vs. Re_T, and (b) same as (a) zoomed on to the intermediate mixing regime during the decay of the flow. Arrows indicate progress in time. Note the abscissa is given in logarithmic scale in (a) and linear scale in (b).

stage between the two cases is due to the difference in the background N^2 value during this period. During the decay stage, with N^2 approximately equal between the two cases, the TKE dissipation ε and the scalar dissipation ε_ρ are directly related by the constant mixing efficiency Γ^d. Figure 19(b) shows the expansion of the intermediate regime in Figure 19(a). The slopes of the best-fit lines indicate the mixing efficiency of $\Gamma^d = 0.4$ for both cases, slightly larger than the values of Γ shown in Figure 15(b). Also, the standard deviations of the fits are considerably smaller for $\tilde{K}_\rho$ when compared to that for K_ρ.

The evolution of $\tilde{K}_\rho$ with respect to Re_T is shown in the Figure 20(a). Figure 20(a) shows the generation and decay stages of $\tilde{K}_\rho$ similar to that in Figure 19(a). In the J_d case, the generation and collapse stages do not fall on top of each other as when Re_b is used. Also, in Figure 16(a), at a fixed value on the abscissa, K_ρ in both cases is larger during the generation stage, but in Figure 20(b), $\tilde{K}_\rho$ in both cases is larger during the decay stage. Figure 20(b) shows a zoom of Figure 20(a) on to the decay stage of the flow. The collapse between the two cases shown in Figure 19(b) is not observed here. The slopes of the best-fit lines in Figure 20(b) are 0.088 in the two-layer case and 0.11 in the J_d case. When Re_T/Ri_g is used to depict the evolution of $\tilde{K}_\rho$, as shown in Figure 21(a), the difference

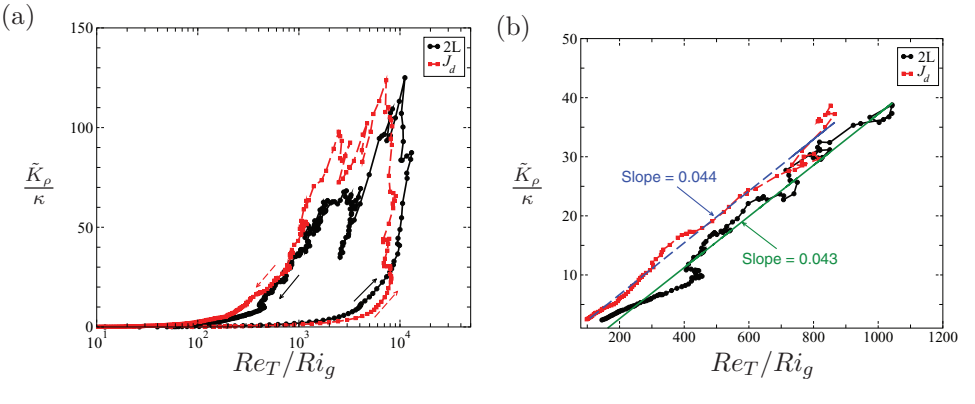

Figure 21. (a) $\tilde{K}_\rho$ vs. Re_T/Ri_g, and (b) same as (a) zoomed on to the intermediate mixing regime during the decay of the flow. Arrows indicate progress in time. Note the abscissa is given in logarithmic scale in (a) and linear scale in (b).

Downloaded by [University of California, San Diego] at 17:42 17 November 2014

in the abscissa between the generation stage and the decay stage is larger relative to that shown in Figure 20(a). Shown in Figure 21(b), the mixing efficiency Γ^d calculated using $10Re_T/Ri_g$ in place of Re_b is equal to 0.43 in the two-layer case and 0.44 in the J_d case, which are slightly larger than 0.4 calculated using Re_b.

7. Conclusions

We have used 3D-DNS to investigate the evolution of turbulent mixing in a stratified shear layer with a relatively high Re, initially $Re = 5,000$. Two cases with different background stratification are considered: (i) two layers of fluid with different density (two-layer case), and (ii) a continuously stratified background (J_d case). The latter has internal waves that propagate away from the mixing layer.

The evolution of the shear layer consists of shear instability, formation of K–H rollers, transition to turbulence, establishment of fully-developed turbulence and, finally, decay toward a laminar state. In previous DNS, transition to turbulence occurs via secondary instability of the braids between the rollers [2]. At the higher Re of the present simulations, not only is there an instability at the braid but also at the vortex core.

Parameterization of the eddy diffusivity, K_ρ, has been explored. The mixing efficiency defined by $\Gamma = -B/\varepsilon$ is often taken to be constant so that the relationship, $K_\rho/\kappa = \Gamma Pr Re_b$ with $Re_b = \varepsilon/\nu N^2$ can be used to infer K_ρ. During the late stage of decaying turbulence in the present flow, Γ is found to be approximately 0.35 while the dissipation-based mixing efficiency defined using the scalar dissipation χ_ρ, is approximately 0.4. An alternate parameterization of K_ρ with respect to the the ratio Re_T/Rig instead of Re_b is also explored. When plotted against Re_b and the ratio Re_T/Rig, the value of the eddy diffusivity is different between growing and decaying stages of stratified shear flow. Furthermore, it is only in the decaying stage, that the two-layer case and J_d case exhibit similar evolution of eddy diffusivity allowing a simple parameterization of K_ρ common to both cases. During this stage, the mixing efficiency defined by the ratio of $-B/\varepsilon$, is approximately 0.35, while the dissipation-based mixing efficiency defined using the scalar dissipation χ_ρ is approximately 0.4.

Comparison of the current DNS at $Re = 5000$ with the results of Pham *et al.* [17] who performed the simulations at $Re = 1280$ indicates that an increase in Re does not alter the mechanism by which internal waves are excited. The direction at which the waves propagate agrees well with the previous study, although the wave energy flux is reduced by approximately 50%. The weaker wave field observed in the current study is due to the earlier breakdown of the K–H rollers to turbulence in the shear layer owing to a high Re effect.

Acknowledgement

We are grateful for the support provided by ONR N000140710133, program monitor Ron Joslin, and ONR N000140810504, program monitor Scott Harper.

References

[1] H.J.S. Fernando, *Turbulent mixing in stratified fluids*, Annu. Rev. Fluid Mech. 23 (1991), pp. 455–493.

[2] W.R. Peltier and C.P. Caulfield, *Mixing efficiency in stratified shear flows*, Annu. Rev. Fluid Mech. 35 (2003), pp. 135–167.

Downloaded by [University of California, San Diego] at 17:42 17 November 2014

[3] G.N. Ivey, K.B. Winters, and J.R. Koseff, *Density stratification, turbulence, but how much mixing?*, Annu. Rev. Fluid Mech. 40 (2008), pp. 169–184.
[4] F.G. Jacobitz, S. Sarkar, and C.W. VanAtta, *Direct numerical simulations of the turbulence evolution in a uniformly sheared and stably stratified flow*, J. Fluid Mech. 342 (1997), pp. 231–261.
[5] J.J. Riley and S.M. deBruynKops, *Dynamics of turbulence strongly influenced by buoyancy*, Phys. Fluids 15 (2003), pp. 2047–2059.
[6] L.H. Shih, J.R. Koseff, G.N. Ivey, and J.H. Ferziger, *Parameterization of turbulent fluxes and scales using homogeneous sheared stably stratified turbulence simulations*, J. Fluid Mech. 525 (2005), pp. 193–214.
[7] C.P. Caulfield and W.R. Peltier, *The anatomy of the mixing transition in homogeneous and stratified free shear layers*, J. Fluid Mech. 413 (2000), pp. 1–47.
[8] J. Werne, T. Lund, B.A. Pattersson-Reif, P. Sullivan, and D.C. Fritts, *CAP phase II simulation for the air force HEL-JTO project: Atmospheric turbulence simulations on NAVO's 3000-processor IBM P4+ and ARL's 2000-processor intel xeon EM64T cluster*, 15th DoD HPC User Group Conference, Nashville, TN, June 2005.
[9] C. Staquet, *Mixing in a stably stratified shear layer: Two- and three-dimensional numerical experiments*, Fluid. Dyn. Res. 27 (2000), pp. 367–404.
[10] K. Winters, P. Lombard, J. Riley, and E.A. D'Asaro, *Available potential energy and mixing in density-stratified fluids*, J. Fluid Mech. 289 (1995), pp. 115–128.
[11] W.D. Smyth and J.N. Moum, *Length scales of turbulence in stably stratified mixing layers*, Phys. Fluids 12 (2000), pp. 1327–1342.
[12] W.D. Smyth and J.N. Moum, *Anisotropy of turbulence in stably stratified mixing layers*, Phys. Fluids 12 (2000), pp. 1343–1362.
[13] W.D. Smyth, J.N. Moum, and D.R. Caldwell, *The efficiency of mixing in turbulent patches: Inferences from direct simulations and microstrucure observations*, J. Phys. Oceanogr. 31 (2001), pp. 1969–1992.
[14] E.J. Strang and H.J.S. Fernando, *Entrainment and mixing in stratified shear flows*, J. Fluid Mech. 428 (2001), pp. 349–386.
[15] K.L. Tse, A. Mahalov, B. Nicolaenko, and H.J.S. Fernando, *Quasi-equilibrium dynamics of shear-stratified turbulence in a model tropospheric jet*, J. Fluid Mech. 496 (2003), pp. 73–103.
[16] B. Sutherland and P. Linden, *Internal wave excitation from stratified flow over thin barrier*, J. Fluid Mech. 377 (1998), pp. 223–252.
[17] H.T. Pham, S. Sarkar, and K.A. Brucker, *Dynamics of a stratified shear layer above a region of uniform stratification*, J. Fluid Mech. 630 (2009), pp. 191–223.
[18] P. Hazel, *Numerical studies of the stability of inviscid stratified shear flows*, J. Fluid Mech. 51 (1972), pp. 39–61.
[19] S. Basak and S. Sarkar, *Dynamics of a stratified shear layer with horizontal shear*, J. Fluid Mech. 568 (2006), pp. 19–54.
[20] K. Brucker and S. Sarkar, *Evolution of an initially turbulent stratified shear layer*, Phys. Fluids 19 (2007), p. 101105.
[21] D.A. Hebert and S.M. de Bruyn Kops, *Predicting turbulence in flows with strong stable stratification*, Phys. Fluids 18 (2006), p. 066602.

Downloaded by [University of California, San Diego] at 17:42 17 November 2014